Research Article Vol. 40, No. 1 / January 2023 / Journal of the Optical Society of America A 35

Journal of the Optical Society of America A
OPTICS, IMAGE SCIENCE, AND VISION

$HE_{1,1}$ mode excited surface plasmon resonance for high-sensitivity sensing by photonic crystal fibers

Yanshu Zeng,[1] Jingwei Lu,[1] Haihao Fu,[1] Xianwen Wu,[2] Lin Yang,[1] Wei Liu,[1] Zao Yi,[3] Qiang Liu,[1] Chunjie Hu,[4] Yan Lv,[1] Paul K. Chu,[5] and Chao Liu[1,*]

[1]School of Physics and Electronic Engineering, Northeast Petroleum University, Daqing 163318, China
[2]School of Chemistry and Chemical Engineering, Jishou University, Jishou 416000, China
[3]Joint Laboratory for Extreme Conditions Matter Properties, Southwest University of Science and Technology, Mianyang 621010, China
[4]Department of Gynaecology and Obstetrics, The Fourth Affiliated Hospital of Harbin Medical University, Harbin 150001, China
[5]Department of Physics, Department of Materials Science and Engineering, and Department of Biomedical Engineering, City University of Hong Kong, Tat Chee Avenue, Kowloon, Hong Kong, China
*Corresponding author: msm-liu@126.com

Received 7 September 2022; revised 11 November 2022; accepted 18 November 2022; posted 21 November 2022; published 5 December 2022

Surface plasmon resonance (SPR) is widely used in photonic crystal fiber sensors. In this work, a photonic crystal fiber sensor based on $HE_{1,1}$ mode excited SPR is designed and analyzed by the finite element method. The maximum wavelength sensitivity, optimal resolution, and amplitude sensitivity of the optical fiber sensor are 24,600 nm/RIU, 4.07×10^{-6} RIU, and 1164.13 RIU^{-1}, respectively, for the refractive index range between 1.29 and 1.39. The sensor has excellent properties and wide application prospects in bimolecular and biochemical sensing, environmental monitoring, food safety, and other fields.

https://doi.org/10.1364/JOSAA.474692

1. INTRODUCTION

Optical sensing is a technology in which changes of external physical parameters are converted into optical signals and then deciphered with demodulation equipment. Common optical sensing techniques include Bragg grating sensing [1], air bubble microcavity sensing [2], optical fiber sensing [3–6], and so on. The principle of optical fiber sensing is total reflection of light. Total reflection occurs when the beam impinges from a light dense medium to light sparse medium and the incident wave angle exceeds the critical angle of total reflection [7]. The single-mode fiber [8] transmits by only one mode. Although the few-mode fiber [9] supports multiple modes of transmission, the transmission distance is short due to intermode dispersion. Therefore, it is imperative to develop more suitable optical fibers. The photonic crystal fiber (PCF) [10–14] has been widely studied because of the high nonlinearity, no cutoff wavelength single-mode transmission, and tunable dispersion. In addition, the shape, size, quantity, spacing, and other parameters of cladding pores can be adjusted flexibly to optimize the characteristics [15].

Different types of PCF sensors have been proposed [16–21], especially the PCF sensor based on surface plasmon resonance (SPR) [22–25] which has attracted extensive attention because of its ability to detect weak signal changes. SPR is a physical and optical phenomenon that occurs at the interface between metals and dielectrics [26]. Free electrons on the surface of the metal vibrate collectively resulting in energy transfer when the incident light meets certain conditions. In different analytes, the photon shift is different and can be used for sensing. For example, Zhang *et al*. [27] proposed a fiber interface waveguide SPR sensor and combined the femtosecond laser writing waveguide technology with SPR effect. Wang *et al*. [28] proposed a new complementary grating structure for plasma refractive index sensing, which has strong resonance in the near-infrared region. In the early stage, SPR was mainly implemented on the prism structure [29], but it is bulky and real-time measurement is difficult. However, real-time detection in a complicated environment can be realized if SPR is adopted by the PCF. Many PCF-SPR sensors have been proposed so far [30–34]. For example, Jiao *et al*. [35] prepared a dual-core photonic crystal fiber by depositing a segmented silver film in the microfluidic channels and Zeng *et al*. [36] described a surface SPR sensor based on the D-shape photonic crystal fiber for a wide refractive index range from 1.15 to 1.36. Shakya *et al*. [37] demonstrated a sensitive bimetallic anisotropic PCF-SPR biosensor with a maximum wavelength sensitivity of 20,000 nm/RIU for x polarization and 18,000 nm/RIU for y polarization.

SPR in these PCF sensors are mostly excited by the $Lp_{0,1}$ mode with the aid of linearly polarized light. However, SPR is

rarely stimulated by the orbital angular momentum (OAM) [38–40] mode based on vortex optical rotation. The beam carrying OAM has a spiral phase structure. Tan *et al*. [41] proved experimentally that the vortex beam can excite the plasmon polaritons on the metal surface. In theory, the topological charge c in the spiral phase factor carried by the OAM mode propagating in the optical fiber can take an unlimited value, so the OAM optical fiber supports an unlimited number of OAM modes and faster mode transmission and has low energy loss and less intermode cross talk [42]. Liu *et al*. [43] proposed a photonic quasi-crystal fiber to excite SPR by the $OAM_{1,1}$ mode but the sensitivity is only about 4000. There is still much room to improve the performance of PCF sensors that are activated by OAM. The $HE_{1,1}$ mode is the basic mode of the OAM mode. Using this mode to excite SPR not only improves the stability of mode transmission in the optical fiber, but also reduces loss and achieves long-distance detection [43]. Other OAM modes can also excite SPR, but the electron movement direction of higher-order OAM mode is inconsistent, which is not conducive to the excitation of SPR. Consequently, it is necessary to develop a high-sensitivity PCF sensor with SPR excited by the OAM mode fundamental mode.

Herein, a PCF-SPR sensor which can detect the refractive index of the analyte in the range of 1.29–1.39 excited by the $HE_{1,1}$ mode is designed and analyzed. In the process of finite element calculation, triangular meshes are used to divide the calculation area. The smaller the mesh, the more accurate the calculation results, but the longer the calculation time. Therefore, a more refined grid is selected according to the complexity of the structure and the operation capability of the equipment. The effects of different structural parameters of the optical fiber on the sensing performance of the PCF-SPR sensor are investigated. Results obtained by the finite element method (FEM) [44,45] show that the average sensitivity of the PCF sensor is as high as 22,430 nm/RIU, the optimal resolution is 4.07×10^{-6} RIU, and the maximum amplitude sensitivity is 1164.13 RIU^{-1}. The proposed sensor can detect a variety of solutions, such as glycerin with a mass fraction of 0.1%–0.2%, sucrose solution with a concentration of 5%–25%, glucose solution with a concentration of 2%–30%, ethanol solution with a concentration of 5%–75%, etc. In addition, the sensor with excellent properties has large potential in oil logging, biosensors, food safety, environmental detection, and other fields.

2. BASIC THEORY AND STRUCTURAL DESIGN

When light travels from an optically dense medium to an optically sparse medium, total reflection can occur. The strength of the evanescent wave decays exponentially with increasing skin depth [46] and the evanescent wave makes the electrons in the metal unevenly distributed. Under the action of Coulombic force, the free electrons on the metal surface vibrate to form surface plasma wave (SPW). Surface plasmon resonance occurs when the propagation constant k_{spw} of the wave and propagation constant k_z of the evanescent wave meet the phase matching conditions shown in Eq. (1), so that the energy of evanescent wave is transferred to SPW [47,48]:

$$k_z = \frac{\omega}{c}\sqrt{\varepsilon_0}\sin\theta = k_{spw}, \tag{1}$$

where ω represents the angular frequency of the incident light, c is the speed of light in vacuum, ε_0 is the dielectric constant of the optical fiber cladding, and θ is the angle of incidence. Most of the energy in the fiber core is coupled to the metal film when the transmission of incident light in the optical fiber meets the phase matching condition, thus stimulating SPR on the metal surface. SPR is very sensitive to the change of refractive indices in the surroundings [49]. The intensity of the formant of the loss spectrum changes when the refractive index of the analyte changes slightly and the resonance wavelength corresponding to the formant redshifts or blueshifts. Therefore, the refractive index of the analyte can be detected by analyzing the change of resonance intensity and the shift of resonance wavelength caused by the change of the refractive index of the analyte. The sensitivity of the PCF-SPR sensor can be calculated from the displacement of the resonance wavelength and change of the refractive index, as shown in Eq. (2) [50]:

$$S_\lambda[\mathrm{nm/RIU}] = \frac{\Delta\lambda_{peak}}{\Delta n_a}, \tag{2}$$

where $\Delta\lambda_{Peak}$ is the displacement of the resonance wavelength and Δn_a represents the change of refractive index.

SPR of the PCF sensor is excited by the fundamental mode of the OAM mode. OAM describes the characteristics of electrons rotating around the transmission axis of electromagnetic waves, which exists in vortex beams with spiral phase. The eigenvector modes in the fiber can be obtained by solving the Maxwell equations. There are four eigenmodes in the fiber: TE mode, TM mode, EH mode, and HE mode. The OAM mode can be regarded as superposition of the odd and even modules of the HE or EH modules of the same order, as shown in Eq. (3) [51,52]:

$$\begin{aligned} OAM^{\pm}_{\pm 1,m} &= HE^{even}_{l+1,m} \pm jHE^{odd}_{l+1,m}, \\ OAM^{\pm}_{\pm 1,m} &= EH^{even}_{l-1,m} \pm jEH^{odd}_{l-1,m}, \end{aligned} \tag{3}$$

where $HE^{even}_{l+1,m}$ and $HE^{even}_{l-1,m}$ represent the even modes of HE and EH, respectively; $HE^{odd}_{l+1,m}$ and $HE^{odd}_{l-1,m}$ represent the odd modes of HE and EH; l is the number of topological charges; m stands for the radial order; the superscript "±" represents the left and right directions of circular polarization; and the subscript "±" is the rotation direction of helical phase. Since the topological charge l of the OAM beam can take an infinite value in theory, OAM fiber supports an unlimited number of OAM modes and faster mode transmission, and more importantly, it has low energy loss.

The optical fiber is more suitable for OAM mode transmission when the optical fiber structure is similar to the OAM mode field phase distribution, so the OAM optical fiber should have a ring structure in design. In addition, the ring PCF fiber helps to support more high-quality OAM modes [52], and the annular arrangement of air holes in the fiber reduces the refractive index of the cladding, making it easier for light to gather in the fiber core for transmission. Therefore, we choose PCF fiber with ring structure for OAM mode transmission.

Figure 1 shows the cross section of the PCF sensor. There are two layers of small air holes with the same radius and one layer of large air holes in the cladding. The center is the solution channel

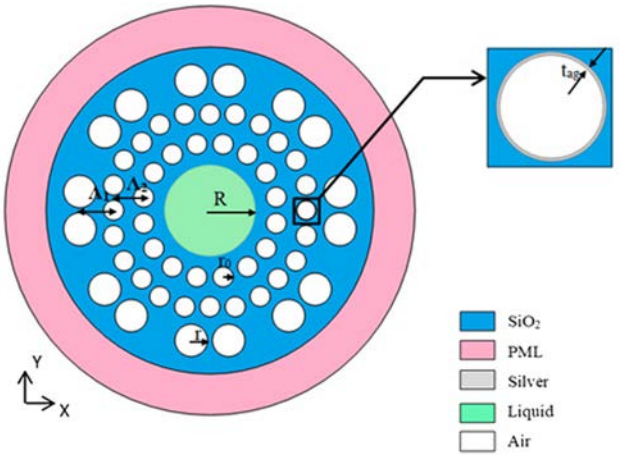

Fig. 1. Cross section of the PCF sensor.

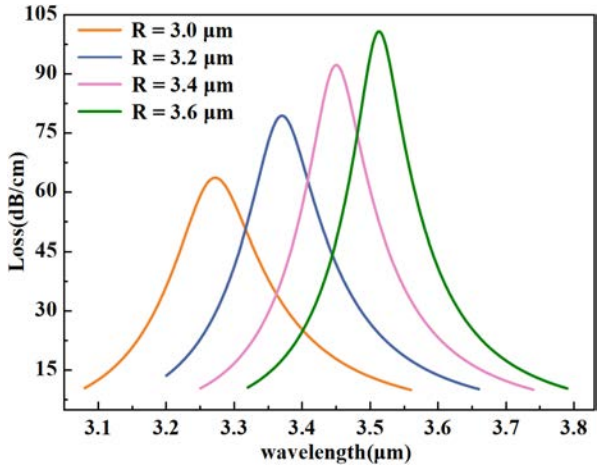

Fig. 2. Loss spectra of the fundamental mode for different channel radii.

to be measured. We coat the second layer of air holes in the direction of the positive half axis of the X axis with a metal film. The materials commonly used in optical fiber sensors are gold and silver. Although silver reacts with oxygen, water, sulfur, and other substances in air more easily, optical fiber sensors used for underground measurement cannot reach oxidation conditions because of the lack of underground oxygen. Moreover, silver is more active than gold, which is easier to excite SPR [53], and the price is relatively lower. Therefore, silver is chosen as the film material. If the silver film is plated on the first layer of the air holes, it is close to the basic mode, which leads to greater loss and shorter detection distance. The silver film is far away from the fundamental mode, if the silver film is coated on the third air hole, and there are weak resonance effects and measurement difficulties. Therefore, in our sensor, a silver film with a thickness of $t_{ag} = 40$ nm is deposited on the second air holes in the positive half-axis direction of the x axis. The dielectric constant is determined by the Drude model [Eq. (4)] [54]:

$$\varepsilon_{Ag}(\omega) = \varepsilon_{\infty} - \frac{\omega_p^2}{\omega(\omega + i\omega_\tau)}, \tag{4}$$

where $\varepsilon_{\infty} = 9.84$, $\omega_p = 1.36 \times 10^{16}$, and $\omega_\tau = 1.018 \times 10^{14}$. The green area in the figure is the solution channel to be tested and the surrounding white area is the air hole. The pink region is the perfectly matched layer which can absorb radiation energy and provide the ideal boundary conditions. The blue area is the optical fiber cladding composed of SiO_2 and the refractive index n is determined by Sellmeier equation [55,56]:

$$n^2 - 1 = \frac{0.6961663\lambda^2}{\lambda^2 - (0.0684043)^2} + \frac{0.4079426\lambda^2}{\lambda^2 - (0.1162414)^2} + \frac{0.897479\lambda^2}{\lambda^2 - (9.896161)^2}, \tag{5}$$

where λ is the wavelength of incident light. The initial structural parameters of the PCF are set as follows: $R = 3$ μm, $\Lambda_1 = 2.4$ μm, $\Lambda_2 = 2.7$ μm, $r = 1.3$ μm, and $r_0 = 0.8$ μm.

In this work, the FEM is utilized to optimize the structural parameters of the sensor. The difficulty of injecting the analyte increases when the channel radius of the solution to be measured is less than 3.0 μm. The annular area between the air holes in the first layer and solution channel is small, when the channel radius of the solution is greater than 3.6 μm. It is not conducive to the generation of orbital angular momentum. Hence, the radius of the channel is set to be between 3.0 and 3.6 μm. Figure 2 presents the loss spectra of the fundamental mode of the sensor when the refractive index of the solution $n_a = 1.36$. The structural parameters are $\Lambda_1 = 2.4$ μm, $\Lambda_2 = 2.7$ μm, $r = 1.3$ μm, and the channel radii R of the solution are 3.0, 3.2, 3.4, or 3.6 μm. The loss of the guided mode can be calculated by Eq. (6) [57]:

$$L = 8.686\frac{2\pi}{\lambda}\mathrm{Im}(n_{\mathrm{eff}}), \tag{6}$$

where $\mathrm{Im}(n_{\mathrm{eff}})$ is the imaginary part of the effective refractive index. As the channel diameter of the solution increases, the resonant wavelength moves toward the long wave direction, and the resonance intensity gradually increases. The value of wear and tear of the optical fiber reaches the maximum and the SPR effect is the strongest when $R = 3.6$ μm. Consequently, the radius of the analyte is chosen to be $R = 3.6$ μm.

The spacing of the air holes also affects the sensor. As the spacing between adjacent air holes becomes larger, light is hard to gather in the fiber core when the air hole interval between the first layer and second layer is greater than 2.6 μm. When the air hole spacing between two layers is less than 2.2 μm, the exchange energy between the core mode and surface plasma mode is less, and phase matching is difficult to take place. As a result, we optimize the distance between the two air holes in the range of 2.2 to 2.6 μm. Figure 3 exhibits the fundamental mode loss spectra for structural parameters of $R = 3.6$ μm, $\Lambda_2 = 2.7$ μm, $r = 1.3$ μm, and the distance between the air holes of the first layer and second layer changes between 2.2 and 2.6 μm. The results show that the resonance peak moves to the long wavelength direction as the air hole spacing between the two layers increases. Afterwards, the loss increases and the resonance wavelength redshifts gradually. The resonance intensity is the largest when $\Lambda_1 = 2.5$ μm. Subsequently, the loss is reduced. This is because the augment of the air hole interval between the two layers causes the energy to gather in the fiber

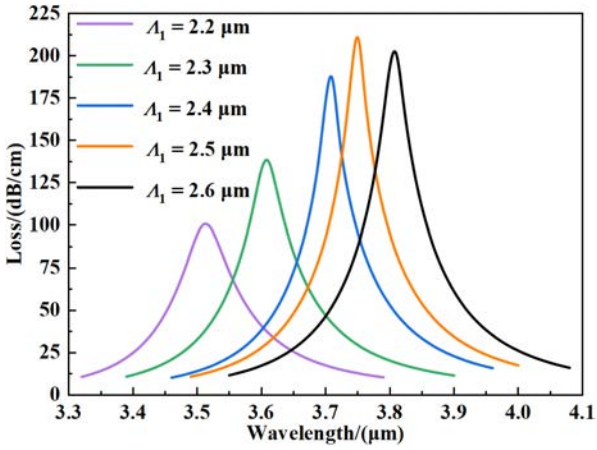

Fig. 3. Loss spectra of the fundamental mode for different air hole spacing between the first layer and second layer.

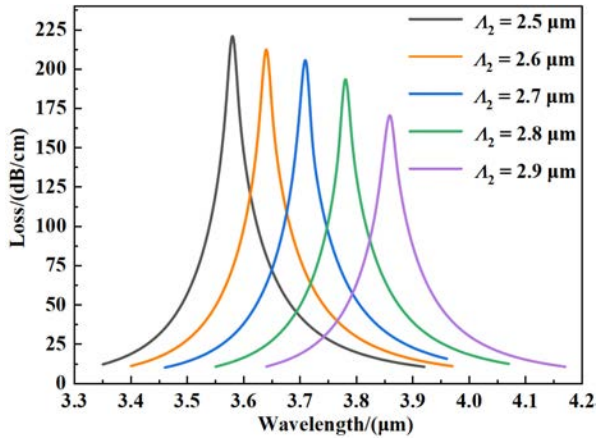

Fig. 4. Loss spectra of the fundamental mode for different air hole spacing between the third layer and second layer.

core and so coupling between the core mode and plasma mode is enhanced. The difference between the resonance peaks of $\Lambda_1 = 2.5$ μm and $\Lambda_1 = 2.4$ μm is small, and the resonance wavelength of $\Lambda_1 = 2.4$ μm is small. Therefore, the air hole gap between the first layer and second layer is chosen to be $\Lambda_1 = 2.4$ μm.

The exchange energy between the core mode and surface plasma mode is less and phase matching is difficult when the distance between the third layer air hole and second layer air hole is below 2.5 μm. The beam cannot concentrate easily in the fiber core when the air hole spacing between the two layers is more than 2.9 μm. Figure 4 shows the loss spectra of the fundamental mode, when the interval between the two layers of air holes is varied from 2.5 to 2.9 μm. As the space between the two layers of air holes expands, the resonance intensity decreases, and the resonance wavelength redshifts. For $\Lambda_2 = 2.5$ μm, the resonance intensity is the maximum. When Λ_2 is less than 2.7 μm, the air hole spacing between the second layer and the third layer is too small, which is difficult to make in practice, so the spacing is chosen as $\Lambda_2 = 2.7$ μm. Based on these structural parameters, the resonance wavelength is shorter and the loss is smaller.

The size of the air holes impacts the properties of the sensor. When the air hole radius is increased, the distance between

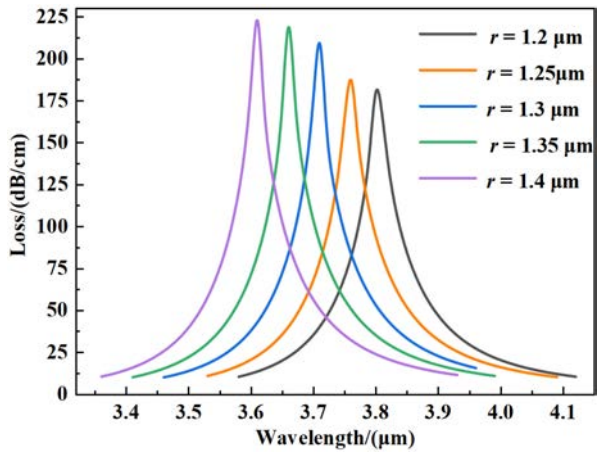

Fig. 5. Loss spectra of the fundamental mode for large air holes with different radii.

adjacent air holes in the same layer becomes smaller, thereby making it easier to concentrate the light in the fiber core. An air hole radius above 1.4 μm or below 1.2 μm will affect the energy exchange between the core mode and surface plasma mode. Here, the semidiameter of the large air holes is chosen to be 1.2, 1.25, 1.3, 1.35, or 1.4 μm for optimization. Figure 5 represents the loss spectra of the fundamental mode when other structural parameters remain unchanged and only the radius of the large air holes is varied. With increasing air hole radius, the resonance wavelength blueshifts and the resonance intensity increases. This is because the large air hole in the third layer has strong restriction on light. The mode field is hard to leak, and more light energy is coupled to the metal film to enhance SPR. Therefore, for ease of manufacture, the air hole radius is chosen to be $r = 1.3$ μm.

The choice of the metal film also affects the resonance strength. Figure 6 presents the loss spectra when the thickness of the silver film is 35, 40, 45, 50, and 55 nm. The resonance intensity increases first and then diminishes and the resonance wavelength blueshifts, with increasing silver film thickness. The SPR strength is not strong when the silver film thickness is less than 40 nm, and the SPR strength gradually decreases when the silver film thickness is greater than 45 nm, so we choose the silver film thickness between 35 and 55 nm for optimization. A silver film that is either too thin or too thick influences the SPR effect, but there is little difference in the resonance intensity when the thickness of the silver film is 45 nm and 50 nm. Hence, t_{ag} is chosen to be 50 nm so that the resonance wavelength is the shortest and the loss is not large.

The change of the radius of the small air hole will also affect the performance of the sensor, but the effect is not significant. The small air radius is too small, which is not conducive to the concentration of light in the fiber core, so we choose to optimize the radius of the small air hole at 0.78 to 0.82 μm. It can be seen from Fig. 7 that the resonance peak has almost no change at the radius of 0.78 to 0.81 μm, so we choose 0.8 μm as the small air hole radius, which is conducive to production and manufacturing.

According to the aforementioned analysis, the optimal structural parameters of the proposed sensor are $R = 3.6$ μm, $\Lambda_1 = 2.4$ μm, $\Lambda_2 = 2.7$ μm, $r = 1.3$ μm, and $t_{ag} = 50$ nm.

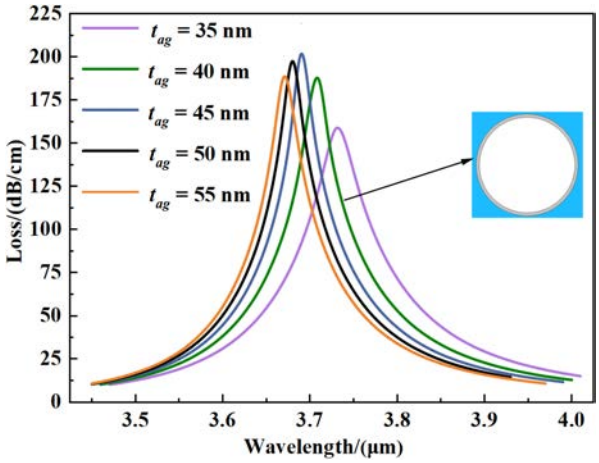

Fig. 6. Loss spectra of the fundamental mode for silver films with different thicknesses.

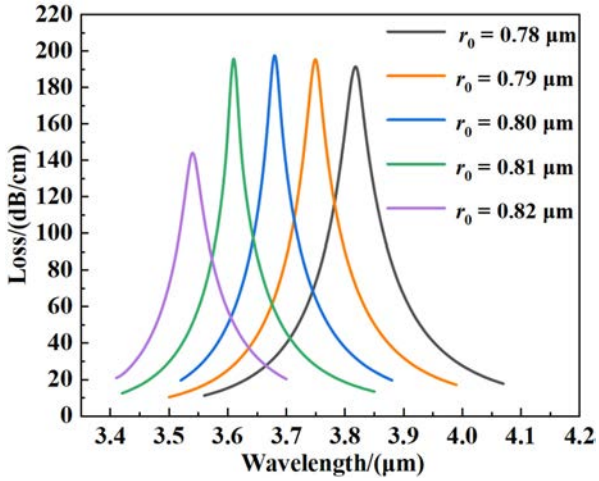

Fig. 7. Relation between the radius of the small air hole and the resonance peak.

In practical production, the solgel method can be used to prepare the optical fibers [15]. First, we make PCF preforms, arrange the metal bars in the mold according to the proposed structure, and then fill the mold with silica gel particles with high PH value, and transform the sol into gel by reducing the PH value. At this time, the gel with microcylindrical air holes can be obtained by removing the metal bar, and then the gel is burned into glass by the thermochemical method. Finally, the PCF preform is drawn into the optical fiber with a certain diameter by the wire drawing process. The reason why the solgel method is more suitable is that this method can freely adjust the size, shape, and position of the air holes [40]. Compared with the stacking method [58], the optical fiber produced by the solgel method using the chemical treatment process to remove impurities is cleaner.

In practical application, the solution detection system based on $HE_{1,1}$ mode excited photonic crystal fiber SPR includes the vortex light source, single-mode fiber, PCF sensor, spectrometer, and computer. In the apparatus, the vortex light source is connected to the single-mode optical fiber and then the single-mode optical fiber is connected to the PCF-SPR sensor by an optical fiber fusion machine. The single-mode optical fiber is connected to the spectrometer (OSA) at the other end of the PCF. When the light source is turned on, the loss spectra will appear on the OSA and is exported to the computer for analysis. The apparatus and process are illustrated in Fig. 8.

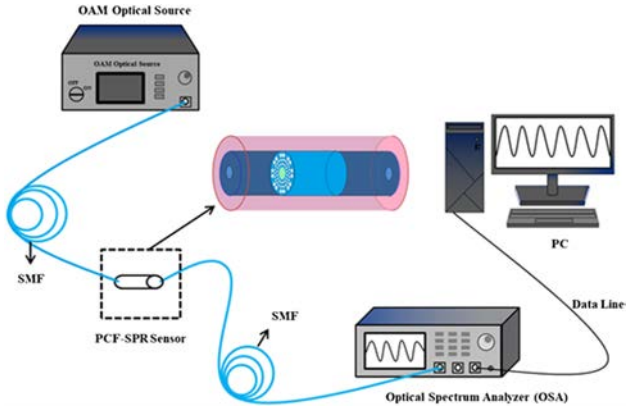

Fig. 8. Schematic of the solution detection system based on $HE_{1,1}$ mode excited photonic crystal fiber SPR.

3. RESULTS AND DISCUSSION

A. Coupling Properties

Figures 9(a)–9(c) show the mode field distributions of the sensor in the x-polarization mode, y-polarization mode, and SPP mode, respectively. The small red arrows indicate the direction of the electric field. The mode field energy of the x-polarization mode and y-polarization mode is mainly concentrated in the fiber core and the mode field energy of the SPP mode is mainly focused on the metal surface. In the x-polarization mode, a small amount of energy is coupled to the metal surface, whereas in the y-polarization mode, the light only gathers in the fiber core and there is no light on the metal surface. In the x-polarization mode, the OAM mode excites SPR, whereas in the y-polarization mode, no SPR is generated. Therefore, the characteristics of the sensor in the x-polarization mode are evaluated.

Figure 10 shows the dispersion and resonance curves of the PCF-SPR optical fiber sensor based on the $HE_{1,1}$ mode at

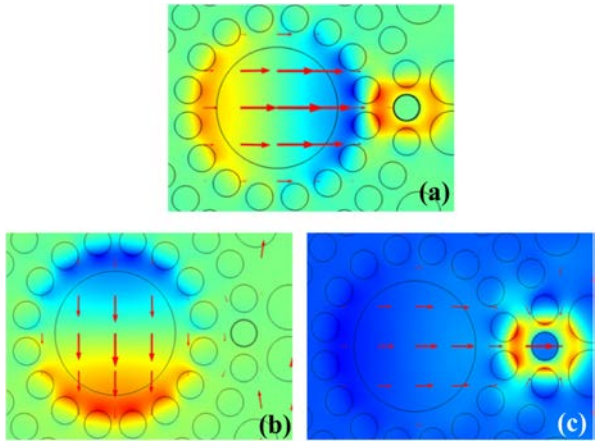

Fig. 9. Mode field distribution of the PCF sensor: (a) x-polarization mode, (b) y-polarization mode, and (c) SPP mode.

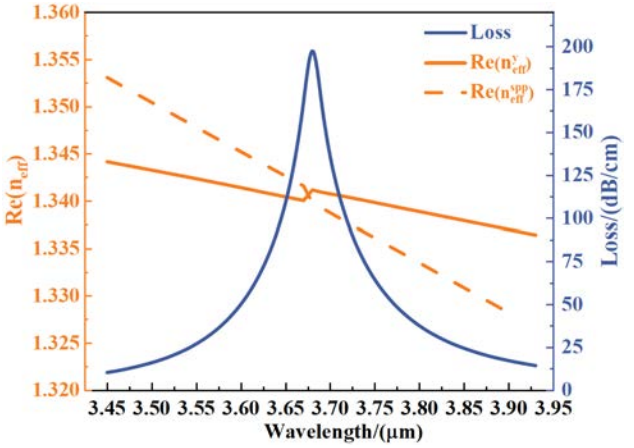

Fig. 10. Dispersion relationship of the plasma mode (orange dashed line) and fundamental mode (orange solid line) and loss spectrum (blue solid line).

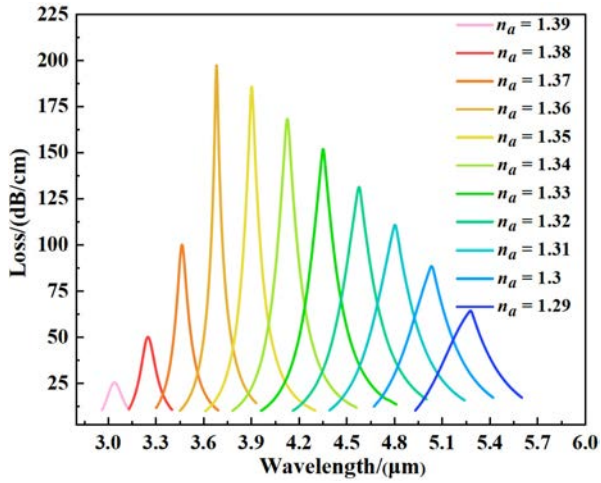

Fig. 11. Fundamental mode loss spectra in different solutions.

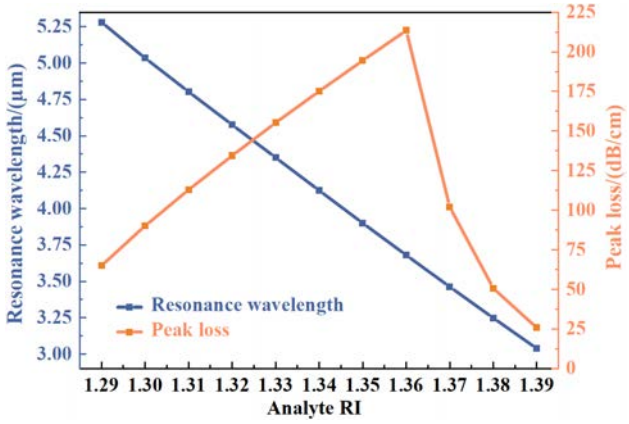

Fig. 12. Resonance wavelength (blue solid line) and loss peak (orange solid line) in different solutions.

different wavelengths when the refractive index of the liquid is 1.36. The orange dotted line represents the dispersion curve of the plasma mode, the orange solid line is the dispersion curve of the base mode, and the blue curve indicates the resonance curve of the base mode. The intersection of the dispersion curves of the base mode and plasma mode coincides with the resonance loss peak. Hence, the base mode and surface plasma mode satisfy the phase matching conditions, and energy coupling between the base mode and plasma mode is the strongest resulting in SPR when the resonance wavelength is 3.68 μm.

B. Wavelength Sensitivity

Figure 11 shows the fundamental mode loss spectra when the refractive index of the fluid changes from 1.29 to 1.39 after the structural parameters of the sensor are optimized. When the refractivity of the liquid increases, the resonance wavelength blueshifts and the loss peak intensity increases first and then declines. Resonance is strongest when the refractive index of the liquid is 1.36 and the resonance wavelength is 3.68 μm. Here, the energy coupling effect between the fundamental mode of the PCF sensor and surface plasma mode is better.

Sensitivity is one of the important parameters [59] and there are two detection methods. The primary method is to monitor the wavelength sensitivity. The resonance wavelength in the spectra will redshift or blueshift when the refractive index of the solution changes. The sensor has high sensitivity, if the refractivity of the liquid changes slightly and the resonant wavelength shifts extensively. The wavelength sensitivity is calculated by Eq. (2).

Figure 12 shows the relationship between the resonant wavelength and loss peak when the refractive index changes from 1.29 to 1.39. The blue solid line indicates the relationship between the resonant wavelength and refractive index, and the orange curve shows that the loss peak varies with the refractive index. The resonance wavelength blueshifts with the refractive index of the solution and the variation between the resonance wavelength and refractive index exhibits a linear relationship. The loss peak increases first and decreases with increasing refractive index grow. When the refractive index of the liquid is 1.36 μm, the resonance intensity reaches the maximum. According to Eq. (2), the average sensitivity of the sensor is 22,430 nm/RIU and the maximum sensitivity is 24,600 nm/RIU.

C. Amplitude Sensitivity

In addition to the shift of the resonant wavelength, the loss peak will also change when the refractive index of the analyte alters. Therefore, the refractive index of the analyte can be detected by the change of the resonant intensity. Amplitude sensitivity is one of the important performances of sensors based on resonance intensity modulation, which is calculated by Eq. (7) [60]:

$$S_A = -\frac{1}{\alpha(\lambda, n_a)} \frac{\Delta\alpha(\lambda, n_a)}{\Delta n_a}, \tag{7}$$

where $\alpha(\lambda, n_a)$ presents the confinement loss. Figure 13 shows the amplitude sensitivity versus refractive index. When the refractive index of the liquid changes from 1.29 to 1.38, the resonance wavelength blueshifts and the amplitude sensitivity increases initially and then declines. The amplitude sensitivity is 1164.13 RIU^{-1}, and the amplitude sensitivity reaches the maximum when the refractive index is 1.35.

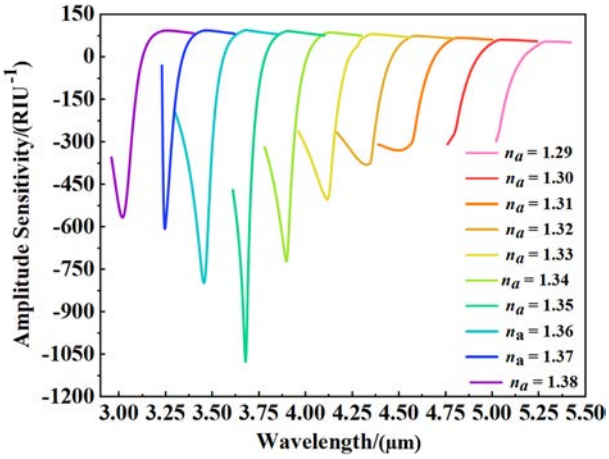

Fig. 13. Amplitude sensitivity of the PCF sensor in different liquids.

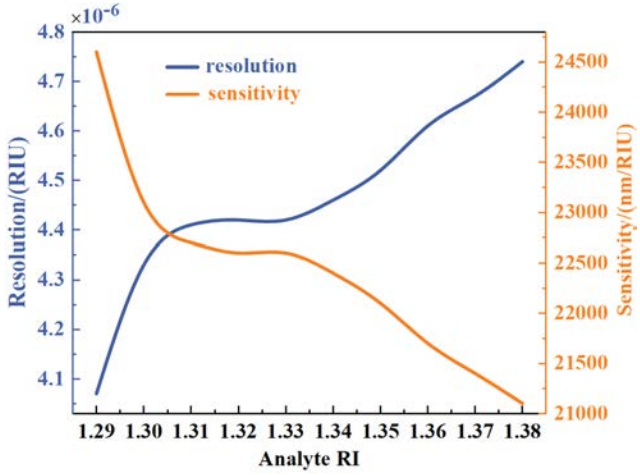

Fig. 14. PCF sensor resolution (blue) and sensitivity (orange) in different solutions.

D. Resolution

Resolution is one of the important parameters as it indicates the ability of the sensor to detect the smallest change. Assuming that a spectral change $\Delta\lambda_{\min} = 0.1$ nm can be detected, the refractive index resolution can be calculated by Eq. (8) [61]:

$$R = \frac{\Delta n_a \Delta\lambda_{\min}}{\Delta\lambda_{\text{peak}}}. \tag{8}$$

Figure 14 exhibits the relationship between the resolution and refractive index. The orange solid line shows the sensitivity change with refractive index and the blue solid line is the variation of resolution for different refractive indices. When the refractive index of the solution is varied from 1.29 to 1.38, the sensitivity of the sensor declines. The sensitivity changes slowly as the refractive index of the liquid changes from 1.31 to 1.33. The trend of resolution is opposite to that of the sensitivity. The resolution ascends slowly when the refractive index of the fluid is changed from 1.31 to 1.33. The resolution goes up rapidly when the refractive index of the liquid is varied in the range of 1.29–1.30 and 1.34–1.38. The resolution of the PCF sensor is the smallest when the refractive index of the solution is 1.29 and the resolution is calculated to be 4.07×10^{-6} RIU by Eq. (8).

E. Figure of Merit

The figure of merit (FOM) describes the overall performance of the PCF sensor and a larger FOM denotes better properties. It is calculated by Eq. (9) [62]:

$$\text{FOM} = \frac{\text{Sensitivity}(S_\lambda)}{\text{FWHM}}, \tag{9}$$

where the full width at half-maximum (FWHM) refers to the width of the loss peak when the height of the loss peak in the spectrum is half. The FWHM represents the working range of the sensor for different refractive indices. Figure 15 shows the relationship between the FOM and FWHM for different refractive indices. The blue curve represents the change of FWHM with refractive indices, and the orange curve indicates the FOM of the PCF sensor. When the refractive index of the

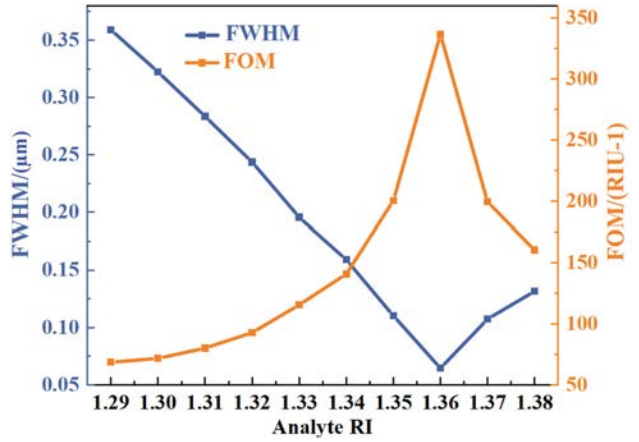

Fig. 15. Curves of FOM (orange) and FWHM (blue) in different solutions.

solution increases, the FWHM declines first and goes up later. The largest FWHM is 0.359 μm when the refractive index of the liquid is 1.29. The minimum value is 0.064 μm when the refractive index of the liquid is 1.36. Therefore, the wavelength range of the resonance curve diminishes as the resonance intensity increases. The trend of the FOM is opposite to that of the FWHM. The FOM increases first and then decreases when the refractivity of the solution is varied from 1.29 to 1.38. The FOM value reaches the maximum of 336.49 RIU^{-1} when the refractive index of the liquid is 1.36.

F. Sensor Length

The sensor length is one of the important parameters to assess the sensor performance and is calculated by Eq. (10) [62]:

$$L = \frac{1}{\alpha(\lambda, n_a)}, \tag{10}$$

where $\alpha(\lambda, n_a)$ indicates the loss value of the PCF sensor at a certain wavelength and the refractive index of the liquid. Figure 16 shows the curve of sensor lengths for different refractive indices. The length of the sensor decreases slowly and then

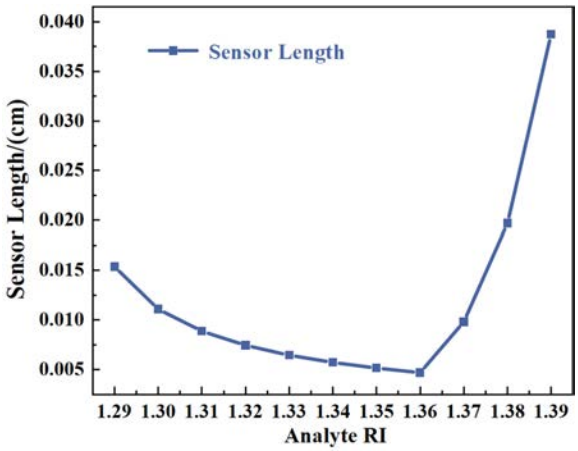

Fig. 16. Sensor lengths in different solutions.

Table 1. Performance Comparison of the Sensing Performance of Different Sensors

Ref.	Detection Range	Wavelength Sensitivity (nm/RIU)	Amplitude Sensitivity (RIU^{-1})	Resolution (RIU)	FOM (RIU^{-1})
[63]	1.33–1.41	12,600	–	7.94×10^{-6}	–
[60]	1.33–1.44	11,200	505.037	8.92×10^{-6}	275
[64]	1.27–1.37	22,400	192	–	127
[65]	1.30–1.38	10000	–	2.0×10^{-5}	–
[66]	1.27–1.32	13 500	–	7.41×10^{-6}	–
Our work	1.29–1.39	24,600	1164.13	4.07×10^{-6}	336.49

increases significantly as the refractive index of the liquid goes up. The length of the sensor is the smallest when the refractivity is 1.36. The maximum sensor length is 0.039 cm when the refractive index is 1.39.

G. Comparison of Sensing Properties

Table 1 compares the main characteristics of PCF sensors in the literature with those of our PCF sensor in terms of the wavelength sensitivity, amplitude sensitivity, resolution, and detection range. Our sensor shows the best wavelength, sensitivity, amplitude sensitivity, and resolution in the refractive index range of 1.29–1.39. The excellent properties illustrate strong energy coupling effect between the core mode and plasma mode in our sensor.

4. CONCLUSION

A high-sensitivity PCF sensor using OAM's fundamental mode to excite SPR is designed and analyzed by the finite element method. The influence of different parameters on the SPR strength of the PCF sensor is discussed. The influence of the size of the solution channel to be measured on the resonance strength is more notable than that of the air hole and the thickness of the silver film. Numerical analysis shows that in the range of refractive index 1.29–1.39, the $HE_{1,1}$ mode can effectively excite SPR and obtain a strong resonant peak at the resonant wavelength. The maximum wavelength sensitivity of the sensor is 24,600 nm/RIU, the optimal resolution is 4.07×10^{-6} RIU, and the amplitude sensitivity is 1164.13 RIU^{-1}. The proposed PCF sensor has excellent sensing performance and has many potential applications in biosensors, environmental monitoring, and food safety.

Funding. Scientific Research Fund of Sichuan Province Science and Technology Department (2020YJ0137); City University of Hong Kong Donation Research Grant (DON-RMG 9229021); City University of Hong Kong Strategic Research (7005505); China Postdoctoral Science Foundation (2020M670881); Natural Science Foundation of Heilongjiang Province (LH2021F007).

Disclosures. The authors declare no conflicts of interest.

Data availability. Data underlying the results presented in this paper are not publicly available at this time but may be obtained from the authors upon reasonable request.

REFERENCES

1. Y. J. Rao, "In-fiber Bragg grating sensors," Meas. Sci. Technol. **8**, 355 (1997).
2. X. Zhang, X. Zhou, and S. Wang, "High-sensitivity fiber-optic Fabry-Perot transverse load sensor based on bubble microcavity," Sens. Actuators, A **335**, 113375 (2022).
3. P. Lu, N. Lalam, and M. Badar, "Distributed optical fiber sensing: review and perspective," Appl. Phys. Rev. **6**, 041302 (2019).
4. T. G. Giallorenzi, J. A. Bucaro, and A. Dandridge, "Optical fiber sensor technology," IEEE Trans. Microwave Theory Tech. **30**, 472–511 (1982).
5. B. Lee, "Review of the present status of optical fiber sensors," Opt. Fiber Technol. **9**, 57–79 (2003).
6. M. Zou, C. Liao, and S. Liu, "Fiber-tip polymer clamped-beam probe for high-sensitivity nanoforce measurements," Light Sci. Appl. **10**, 171 (2021).
7. B. L. Mojet, S. D. Ebbesen, and L. Lefferts, "Light at the interface: the potential of attenuated total reflection infrared spectroscopy for understanding heterogeneous catalysis in water," Chem. Soc. Rev. **39**, 4643–4655 (2010).
8. L. B. Jeunhomme, *Single-Mode Fiber Optics: Principles and Applications* (2019).
9. P. Sillard, M. Bigot-Astruc, and D. Boivin, "Few-mode fiber for uncoupled mode-division multiplexing transmissions," in *37th European Conference and Exhibition on Optical Communication* (IEEE, 2011), pp. 1–3.
10. E. Liu, S. Liang, and J. Liu, "Double-cladding structure dependence of guiding characteristics in six-fold symmetric photonic quasi-crystal fiber," Superlattices Microstruct. **130**, 61–67 (2019).
11. E. Liu, W. Tan, B. Yan, J. Xie, R. Ge, and J. Liu, "Robust transmission of orbital angular momentum mode based on a dual-cladding photonic quasi-crystal fiber," J. Phys. D **52**, 325110 (2019).
12. C. Li, B. Yan, and J. Liu, "Refractive index sensing characteristics in a D-shaped photonic quasi-crystal fiber sensor based on surface plasmon resonance," J. Opt. Soc. Am. A **36**, 1663–1668 (2019).
13. E. Liu, W. Tan, B. Yan, J. Xie, R. Ge, and J. Liu, "Broadband ultra-flattened dispersion, ultra-low confinement loss and large effective mode area in an octagonal photonic quasi-crystal fiber," J. Opt. Soc. Am. A **35**, 431–436 (2018).
14. B. Yan, A. Wang, E. Liu, W. Tan, J. Xie, R. Ge, and J. Liu, "Polarization filtering in the visible wavelength range using surface plasmon resonance and a sunflower-type photonic quasi-crystal fiber," J. Phys. D **51**, 155105 (2018).
15. H. Fu, C. Liu, and C. Hu, "Circular photonic crystal fiber supporting 118 orbital angular momentum modes transmission," Opt. Eng. **60**, 076102 (2021).
16. A. A. Rifat, G. A. Mahdiraji, and Y. M. Sua, "Surface plasmon resonance photonic crystal fiber biosensor: a practical sensing approach," IEEE Photonics Technol. Lett. **27**, 1628–1631 (2015).

17. W. Liu, Y. Shid, and Z. Yi, "Surface plasmon resonance chemical sensor composed of a microstructured optical fiber for the detection of an ultra-wide refractive index range and gas-liquid pollutants," Opt. Express **29**, 40734–40747 (2021).
18. R. Otupiri, E. K. Akowuah, and S. Haxha, "A novel birefringent photonic crystal fiber surface plasmon resonance biosensor," IEEE Photonics J. **6**, 6801711 (2014).
19. W. Liu, C. Hu, and L. Zhou, "A highly sensitive D-type photonic crystal fiber infrared sensor with indium tin oxide based on surface plasmon resonance," Mod. Phys. Lett. B **36**, 2150499 (2022).
20. A. A. Rifat, G. A. Mahdiraji, and Y. G. Shee, "A novel photonic crystal fiber biosensor using surface plasmon resonance," Procedia Eng. **140**, 1–7 (2016).
21. W. Liu, C. Hu, and L. Zhou, "A square-lattice D-shaped photonic crystal fiber sensor based on SPR to detect analytes with large refractive indexes," Phys. E **138**, 115106 (2022).
22. H. Chen, Z. Chen, H. Yang, L. Wen, Z. Yi, Z. Zhou, B. Dai, J. Zhang, X. Wu, and P. Wu, "Multi-mode surface plasmon resonance absorber based on dart-type single-layer grapheme," RSC Adv. **12**, 7821–7829 (2022).
23. F. Zhao, J. Lin, Z. Lei, Z. Yi, F. Qin, J. Zhang, L. Liu, X. Wu, W. Yang, and P. Wu, "Realization of 18.97% theoretical efficiency of 0.9 μm thick C-Si/ZnO heterojunction ultrathin-film solar cells via surface plasmon resonance enhancement," Phys. Chem. Chem. Phys. **24**, 4871–4880 (2022).
24. R. B. M. Schasfoort, *Handbook of Surface Plasmon Resonance* (Royal Society of Chemistry, 2017).
25. F. Zhou, F. Qin, Z. Yi, W.-T. Yao, Z. Liu, X. Wu, and P. Wu, "Ultra-wideband and wide-angle perfect solar energy absorber based on Ti nanorings surface plasmon resonance," Phys. Chem. Chem. Phys. **23**, 17041–17048 (2021).
26. J. Chen, Y. Kuang, and P. Gu, "Strong magnetic plasmon resonance in a simple metasurface for high-quality sensing," J. Lightwave Technol. **39**, 4525–4528 (2021).
27. Y. Zhang, C. Liao, and C. Lin, "Surface plasmon resonance refractive index sensor based on fiber-interface waveguide inscribed by femtosecond laser," Opt. Lett. **44**, 2434–2437 (2019).
28. X. Wang, J. Zhu, and Y. Xu, "A novel plasmonic refractive index sensor based on gold/silicon complementary grating structure," Chin. Phys. B **30**, 024207 (2021).
29. H. R. Gwon and S. H. Lee, "Spectral and angular responses of surface plasmon resonance based on the Kretschmann prism configuration," Mater. Trans. **51**, 1150–1155 (2010).
30. C. Liu, J. Wang, and X. Jin, "Near-infrared surface plasmon resonance sensor based on photonic crystal fiber with big open rings," Optik **207**, 164466 (2020).
31. Q. Liu, S. Li, and H. Li, "Broadband single-polarization photonic crystal fiber based on surface plasmon resonance for polarization filter," Plasmonics **10**, 931–939 (2015).
32. G. An, S. Li, and X. Yan, "High-birefringence photonic crystal fiber polarization filter based on surface plasmon resonance," Appl. Opt. **55**, 1262–1266 (2016).
33. A. Hassani, B. Gauvreau, and M. F. Fehri, "Photonic crystal fiber and waveguide-based surface plasmon resonance sensors for application in the visible and near-IR," Electromagnetics **28**, 198–213 (2008).
34. Z. Yang, L. Xia, and C. Li, "A surface plasmon resonance sensor based on concave-shaped photonic crystal fiber for low refractive index detection," Opt. Commun. **430**, 195–203 (2019).
35. S. Jiao, S. Gu, and H. Fang, "Analysis of dual-core photonic crystal fiber based on surface plasmon resonance sensor with segmented silver film," Plasmonics **14**, 685–693 (2019).
36. W. Zeng, Q. Wang, and L. Xu, "Plasmonic refractive index sensor based on D-shaped photonic crystal fiber for wider range of refractive index detection," Optik **223**, 165463 (2020).
37. A. K. Shakya, A. Ramola, and S. Singh, "Design of an ultra-sensitive bimetallic anisotropic PCF SPR biosensor for liquid analytes sensing," Opt. Express **30**, 9233–9255 (2022).
38. C. Liu, H. Fu, and C. Hu, "Optimization of photonic crystal fibers for transmission of orbital angular momentum modes," Opt. Quantum Electron. **53**, 1 (2021).
39. H. Fu, M. Zhu, and C. Liu, "Photonic crystal fiber supporting 394 orbital angular momentum modes with flat dispersion, low nonlinear coefficient, and high mode quality," Opt. Eng. **61**, 026111 (2022).
40. H. Fu, Z. Yi, and Y. Shi, "Circular anti-resonance fibre supporting orbital angular momentum modes with flat dispersion, high purity and low confinement loss," J. Mod. Opt. **68**, 784–791 (2021).
41. P. S. Tan, X. C. Yuan, and J. Lin, "Surface plasmon polaritons generated by optical vortex beams," Appl. Phys. Lett. **92**, 111108 (2008).
42. B. Kuiri, B. Dutta, and N. Sarkar, "Design and optimization of photonic crystal fiber with low confinement loss guiding 98 OAM modes in THz band," Opt. Fiber Technol. **68**, 102752 (2022).
43. E. Liu, B. Yan, and H. Zhou, "OAM mode-excited surface plasmon resonance for refractive index sensing based on a photonic quasi-crystal fiber," J. Opt. Soc. Am. B **38**, F16–F22 (2021).
44. K. J. Bathe, *Finite Element Method*, Wiley Encyclopedia of Computer Science and Engineering (John Wiley & Sons, 2007), pp. 1–12.
45. H. C. Huang and A. S. Usmani, "Finite element method," in *Finite Element Analysis for Heat Transfer* (Springer, 1994), pp. 21–47.
46. J. E. Reid and J. C. Macnaem, "Doubling the effective skin depth with a local source," Geophysics **64**, 732–738 (1999).
47. A. Yasli, "Cancer detection with surface plasmon resonance-based photonic crystal fiber biosensor," Plasmonics **16**, 1605–1612 (2021).
48. Z. Yan, X. Lu, and W. Du, "Ultraviolet graphene ultranarrow absorption engineered by lattice plasmon resonance," Nanotechnology **32**, 465202 (2021).
49. L. Chen, W. Zhang, and Z. Zhang, "Design for a single-polarization photonic crystal fiber wavelength splitter based on hybrid-surface plasmon resonance," IEEE Photonics J. **6**, 2200909 (2014).
50. C. Liao, C. Xiong, and J. Zhao, "Design and realization of 3D printed fiber-tip microcantilever probes applied to hydrogen sensing," Light Adv. Manuf. **3**, 1–11 (2022).
51. H. Fu, C. Liu, and Z. Yi, "A new technique to optimize the properties of photonic crystal fibers supporting transmission of multiple orbital angular momentum modes," J. Opt. (2022).
52. H. Fu, Y. Shi, and Z. Yi, "Effects of air holes in the cladding of photonic crystal fibers on dispersion and confinement loss of orbital angular momentum modes," Opt. Quantum Electron. **54**, 353 (2022).
53. A. A. Rifat, G. A. Mahdiraji, and D. M. Chow, "Photonic crystal fiber-based surface plasmon resonance sensor with selective analyte channels and graphene-silver deposited core," Sensors **15**, 11499–11510 (2015).
54. L. Qi, B. I. Lee, and S. Chen, "High-dielectric-constant silver–epoxy composites as embedded dielectrics," Adv. Mater. **17**, 1777–1781 (2005).
55. C. Liu, J. Lü, and W. Liu, "Overview of refractive index sensors comprising photonic crystal fibers based on the surface plasmon resonance effect," Chin. Opt. Lett. **19**, 102202 (2021).
56. Z. Zheng, Y. Luo, H. Yang, Z. Yi, J. Zhang, Q. Song, W. Yang, C. Liu, X. Wu, and P. Wu, "Thermal tuning of terahertz metamaterial properties based on phase change material vanadium dioxide," Phys. Chem. Chem. Phys **24**, 8846–8853 (2022).
57. X. Wang, J. Zhang, and J. Zhu, "Refractive index sensing of double Fano resonance excited by nano-cube array coupled with multilayer all-dielectric film," Chin. Phys. B **31**, 024210 (2021).
58. M. R. Islam, M. M. I. Khan, and S. Siraz, "Design and analysis of a QC-SPR-PCF sensor for multipurpose sensing with supremely high FOM," Appl. Nanosci. **12**, 29–45 (2022).
59. C. Dou, X. Jing, and S. Li, "A photonic crystal fiber polarized filter at 1.55 μm based on surface plasmon resonance," Plasmonics **11**, 1163–1168 (2016).
60. Q. M. Kamrunnahar, J. R. Mou, and M. Momtaj, "Dual-core gold coated photonic crystal fiber plasmonic sensor: design and analysis," Results Phys. **18**, 103319 (2022).
61. D. Li, W. Zhang, and H. Liu, "High sensitivity refractive index sensor based on multicoating photonic crystal fiber with surface plasmon resonance at near-infrared wavelength," IEEE Photonics J. **9**, 6801608 (2017).
62. S. Singh and Y. K. Prajapati, "Dual-polarized ultrahigh sensitive gold/MoS_2/graphene based D-shaped PCF refractive index sensor in visible to near-IR region," Opt. Quantum Electron. **52**, 1 (2022).

63. T. Li, L. Zhu, and X. Yang, "A refractive index sensor based on H-shaped photonic crystal fibers coated with Ag-graphene layers," Sensors **20**, 741 (2022).
64. Y. E. Monfared and M. Qasymeh, "Plasmonic biosensor for low-index liquid analyte detection using graphene-assisted photonic crystal fiber," Plasmonics **16**, 881–889 (2021).
65. V. Kaur and S. Singh, "D-shaped photonic crystal fiber based surface plasmon resonance sensor using dual coating of metal oxide for healthcare applications," in *2021 IEEE 16th Nanotechnology Materials and Devices Conference (NMDC)* (IEEE, 2021), pp. 1–4.
66. F. Wang, C. Liu, and Z. Sun, "A highly sensitive SPR sensors based on two parallel PCFs for low refractive index detection," IEEE Photonics J. **10**, 7104010 (2018).